Tedim, J.; Bastos, A.C.; Kallip, S.; Zheludkevich, M.L.; Ferreira, M.G.S.:
Corrosion protection of AA2024-T3 by LDH conversion films. Analysis of SVET results
In: Electrochimica Acta (2016) Elsevier

DOI: 10.1016/j.electacta.2016.05.134

Corrosion protection of AA2024-T3 by LDH conversion films. Analysis of SVET results.

J. Tedim[1,§,*], A.C. Bastos[§], S. Kallip[1,§], M.L. Zheludkevich[1,§,¥], M.G.S. Ferreira[1,§]

[§]CICECO – Aveiro Institute of Materials, Departamento de Engenharia de Materiais e Cerâmica and Universidade de Aveiro, 3810-193 Aveiro, Portugal

[¥] Institute of Materials Research, Helmholtz-Zentrum Geesthacht, Centre for Materials and Coastal Research GmbH, Max-Planck-Str. 1, 21502 Geesthacht, Germany

(*) Corresponding author: joao.tedim@ua.pt

(1) ISE member

Abstract

In this work the protective effect of layered double hydroxide (LDH) films directly grown on the surface of 2024-T3 aluminium alloy is investigated using electrochemical impedance spectroscopy (EIS) and the scanning vibrating electrode technique (SVET). The SVET results focused on the localised nature of the corrosion process and are in agreement with the global response measured by EIS. Furthermore, the evolution of active corrosion protection rendered by LDH films is surveyed at microscale for the first time for long immersion periods in NaCl solution and in the presence of induced defects. The quantitative information provided by SVET is discussed and a parameter to describe the degree of corrosion localisation is introduced based on LDH systems.

Keywords:

SVET; 2024-T3 aluminium alloy; neutral inhibition; pitting corrosion; LDH films.

1. Introduction

The use of conversion films for protection of aluminium alloys has been widely investigated for aeronautical applications. The toxicity and environmental concerns of technologies based on Cr-derived systems have prompted material scientists to come up with more environmentally friendly solutions, including conversion films based on rare-earth metals [1, 2], sol-gel technologies [3-5], conducting polymers [6, 7] and layered double hydroxides (LDHs) [8-10].

In previous works, we reported a facile method for growing LDHs on aluminium alloys and intercalation of vanadates for corrosion inhibition [9,11,12], as sketched in Figure 1. The influence of different parameters such as concentration of reactants [11] and the effect of surface pre-treatment on the growth of LDH films [12] was investigated in detail. The results showed that a compromise between the stability of the oxide film and the extent of LDHs, grown on the top of it, is needed to achieve the best performance [12].

The electrochemical studies reported before were mostly based on techniques that give an ‘average’ response of the sample’s surface. Given the localised nature of the corrosion of 2024 aluminium alloy and heterogeneity of the LDH film, the use of localised techniques, namely SVET, can unveil the corrosion progress at the micro-scale, ultimately bringing novel insights into the understanding of corrosion protection conferred by LDH films. Therefore, the main objectives of this work were (i) to investigate how the LDH films perform for long immersion times in NaCl electrolyte and (ii) how the SVET technique can help to visualise the evolution of localised corrosion activity sustained by the AA2024-T3 alloy, in the absence and presence of induced defects. Moreover, SVET data were analysed in an attempt to extract more

information than the usual obtained just by a qualitative or semi-quantitative comparison of current density maps.

Figure 1

2. Material and methods

2.1. Materials.

All the chemicals were obtained from Aldrich, Fluka, and Riedel-de Haen, with at least ≥98% of ground substance, and used as received. Specimens of 2024-T3 aluminium alloy with the following composition were used: Cu 3.8-4.9 %, Mg 1.2-1.8 %, Mn 0.3-0.9 %, Fe 0.5 %, Si 0.5 %, Zn 0.25%, Ti 0.15 %, Cr 0.1 %, other 0.15 %, balance Al.

2.2. Preparation of metallic substrates.

The AA2024-T3 plates were firstly washed with deionised water and ethanol, dried with compressed air and then immersed in 0.1 M NaOH for 120 s at room temperature. Afterwards, the plates were rinsed in deionised water and immersed in 0.1 M HNO_3 for 480 s. Finally, the specimens were washed with deionised water, ethanol and dried.

2.3. Synthesis of LDH conversion films.

The LDH conversion films were synthesised as described previously in references [9, 11] (recall Fig. 1). Succinctly, AA2024-T3 plates were immersed in a 5 mM $Zn(NO_3)_2$ solution (pH~7) for a few hours at high temperature (T~ 100 ºC). Under these conditions, Zn(2)-Al-NO_3 LDH films were grown on the surface of the aluminium alloy substrates (referred as **LDH-NO_3** in the remaining text). Subsequently, the plates were washed with ultrapure H_2O, ethanol, and dried in air. Zn(2)-Al-VO_x LDH (denoted **LDH-VO_x** in the remaining text) was obtained by immersing Zn(2)-Al-NO_3 coated

plates in $NaVO_3$ solution with pH 8-9 for a few hours under hydrothermal treatment (T~ 50 ºC). The pH control was important to obtain the vanadate species with proper corrosion inhibiting properties, as shown by Buchheit [13].

2.4. Characterisation procedures.

The morphology and composition of LDH films were characterised by scanning electron microscopy coupled with energy dispersive spectroscopy (SEM-EDS), using a Hitachi SU-70 Schottky emission scanning electron microscope with an electron beam energy of 15 kV and a Quantax 400 energy dispersive X-ray spectrometer from Bruker.

The EIS measurements were carried out in a three-electrode cell with a saturated calomel reference electrode, a platinum foil counter electrode and the aluminium alloy sample as the working electrode (exposed area of ca. 3 cm^2). The testing medium was a 0.05 M NaCl aqueous solution (10 mL volume). The cell was placed in a Faraday cage to avoid the interference of external electromagnetic fields and the measurements were performed using a Gamry FAS2 Femtostat with PCI4 Controller. A 10 mV rms sinusoidal perturbation was swept in the 10^5 to 10^{-2} Hz frequency range, with 10 points per frequency decade. All the spectra were recorded at open circuit potential. The impedance data were fitted using equivalent circuits based on RC elements presented and discussed in reference [11], where pure capacitances were replaced by constant phase elements, CPEs. The quality of fittings was evaluated by the values of χ^2.

The SVET measurements were performed on samples of 1 cm^2 glued to an epoxy holder. A mixture of beeswax and colophony was used to insulate each sample leaving a window of a few mm^2 exposed to the testing solution, 0.05 M NaCl. The area inside the window was the only part of the sample exposed to solution and was completely scanned and photographed by the SVET system. Adhesive tape applied around the

epoxy support made the solution reservoir. The volume was 5 mL and the thickness of solution above the surface was ~7 mm. The measurements were performed with an Applicable Electronics Inc. (USA) instrument and under the control of the ASET software from ScienceWares (USA). The vibrating microelectrode had a 10 µm spherical platinum black tip and vibrated at 88 Hz with amplitude of 10 µm at an average distance of 200 µm from the surface of the sample. Each scan comprised 40 x 40 points and took about 11 minutes to be completed.

3. Results

3.1. Surface analysis

Figure 2 presents a SEM image and corresponding EDS maps of Zn, Al and N of the AA2024-T3 surface after the growth of LDH films. The surface is covered by a thin film separated by micrometre-sized islands where LDH are concentrated, as inferred from Zn and N maps. This structuration of the surface is attributed to a differentiated dissolution of Al^{3+} from the substrate. The island-like morphology occurs above the intermetallic phases (Fig. 1), where a weaker oxide layer leads to a relatively higher dissolution of Al^{3+} from the intermetallics, which promotes the preferential growth of LDH. The layered double hydroxide structure of the films has been confirmed in previous works by X-ray diffraction [9, 11, 12].

Figure 2

3.2. Electrochemical impedance spectroscopy

The electrochemical behaviour of the AA2024-T3/LDH system in aqueous NaCl solution was studied by electrochemical techniques, namely EIS and SVET.

The EIS data analysis for LDH films was described in detail in a recently published work in this journal [11], where we provided the rationale for the equivalent circuits used with the meaning of the different time constants and quality of fitting. In the present work we use the same approach for the interpretation of EIS data of LDH films prepared under similar conditions.

Figure 3 shows the Bode and Nyquist representations of EIS spectra acquired during one month of immersion in 0.05 M NaCl solution. The main reason for choosing a relatively dilute NaCl solution was to produce a lower corrosion rate, thereby facilitating identification of features not resolved otherwise.

The impedance of each sample did not change significantly during the testing period, though the behaviour of different systems was remarkably distinct. In the case of the reference system (bare AA2024-T3 substrate), two time constants were detected, one at intermediate frequencies ($\approx 10^{0}$ Hz) and another, not totally defined, at low frequencies ($\approx 10^{-2}$ Hz). The first was ascribed to the corrosion process (response of double layer capacitance, CPE_{dl}, in parallel with charge transfer resistance, R_{ct}) while the second was associated to a diffusion-controlled process [11]. The equivalent electric circuit of Figure 4 a) can be used to represent the impedance response of this system. In the case of systems with LDH films, the impedance at low frequencies was one order of magnitude higher than the bare substrate and the response can be fitted by an equivalent electric circuit with three time constants (Figure 4b) [11]. The time constant occurring at higher frequencies ($>10^{3}$ Hz) is due to the LDH film response, represented by a CPE_{LDHs} in parallel with the pore resistance of the LDH film (R_{LDHs}), while the second one, appearing at intermediate frequencies ($\approx 10^{0}$-10^{1} Hz), is associated with the aluminium oxide film always present on the surface of the alloy and represented by a CPE_{ox} in

parallel with the oxide resistance (R_{ox}). The third time constant ($\approx 10^{-1}$Hz) is attributed to electrochemical activity related with corrosion process (R_{ct} and CPE_{dl}).

Figure 3

Figure 4

Figure 5 shows the evolution of the resistive parameters of the three systems obtained by numerical fitting of the impedance spectra. The resistance of the LDH film is around 1 kΩ cm^2 for the system containing vanadates and is 10-100 times lower for the one with nitrate as intercalated ion. Nonetheless, the R_{ct} of **LDH-NO$_3$** systems is in the range of 1 MΩ cm^2, i.e. two orders of magnitude higher than the uncoated substrate. The R_{ct} of **LDH-VO$_x$** is even higher, being detected at lower frequencies only after 300 hours of immersion. These results confirm the action of LDH film as a protective layer against corrosion of the substrate, particularly when vanadates are present, and fully agree with previous results [9, 11, 12]. The resistance to corrosion can be ranked by the values of R_{ct} (inversely proportional to the corrosion rate): **LDH-VO$_x$** > **LDH-NO$_3$** > **AA2024-T3**.

Figure 5

3.3. Scanning Vibrating Electrode Technique

EIS gives the averaged global response of the samples. Complementary information can be obtained by localised techniques, namely with the SVET, which provides the distribution and magnitude of anodic and cathodic activity on the corroding surface. Figure 6 presents the SVET maps and corresponding optical photographs of the three systems immersed in 0.05 M NaCl for one month. The maps and photographs capture the entirety of the area exposed to solution in each system. The maps corresponding to bare AA2024-T3 substrate (Fig. 6a) show corrosion currents already at very early stages

of immersion. Several anodic spots are detected (red coloured regions), an indication of localised activity, while the cathodic activity (blue colour) spreads over the remaining surface. Comparing the maps acquired at different times, some pits remained active during the whole period of immersion. Furthermore, the optical photographs corroborate the electrochemical activity measured by SVET: several pits appeared on the surface and the formation of corrosion products was already visible in the first day of immersion.

When LDH films intercalated with NO_3^- are grown on the aluminium surface, the electrochemical activity decreases remarkably. In this case, only one active anodic pit was detected during one month - Figure 6 b. The **LDH-NO_3** film is a physical barrier which limits the access of aggressive species and O_2 to the substrate and decreases the available exposed metal surface for reaction. At the same time, LDHs have the ability to entrap chlorides as discussed in a previous work [9]. Some level of corrosion retardation may also be attributed to both NO_3^- and Zn^{2+}, as described in the literature. Nitrates have been reported as species displaying inhibiting properties on aluminium alloys [14], even when intercalated in LDH-based powders [15]. On the other hand, Zn^{2+} entrapped in the LDHs films during the synthesis step can work as cathodic inhibitor by precipitating as hydroxides on the cathodic areas, as pointed out by Buchheit and colleagues [16].

In the case of **LDH-VO_x** films, no corrosion currents were detected by SVET - Figure 6 c. The optical photographs show the appearance of one pit after 1 week of immersion. Nevertheless, the current associated with this feature has to be quite low because it was not detected by SVET. At the same time, the amount of corrosion products accumulated during one month of testing was very small. In addition to the physical barrier, the corrosion resistance is possibly due to the low level of cathodic activity suppressed by

vanadate released from LDHs. Vanadates are known as effective inhibitors for protection of aluminium alloys against corrosion [13, 17, 18]. The inhibition is not attributed to their oxidative power, as much as to their ability to adsorb on the surface in unaltered oxidation state. This action was found to be pH dependent [13] and works by inhibiting the oxygen reduction reaction.

Figure 6

A comparison between samples is shown in Figure 7, with 3D maps of the systems after one month of immersion using the same current density scale. A ranking of corrosion resistance can be established considering as criterion either the maximal anodic current peak, the number of anodic peaks or the total anodic current. In all cases the order of corrosion resistance is **LDH-VO_x** > **LDH-NO_3** >> **AA2024-T3**.

Figure 7

The good performance of the **LDH-VO_x** system in NaCl solution remains even when artificial defects are produced on the film. Figure 8 depicts current density maps and the corresponding optical photographs for an AA2024-T3 sample coated with **LDH-VO_x,** after two pin-holes were made in the centre of the sample. Interestingly, no current densities were detected during the first days of immersion and the optical images reveal just a small amount of corrosion products produced during one month of testing. This may be due to the prompt release of vanadates and the fast inhibitive action on the corrosion process at the defects. It is known that LDHs exchange the intercalated species within minutes [19], so vanadates may be available to protect the defects already when the first map is acquired after 30 minutes of immersion. The protection lasts over

several days, which is evidenced by the corrosion being restricted to the defects and the level of attack remaining small during the complete testing period. The current density of **LDH-VO_x** with defects very much resembles that of the intact film, which underlines the superior performance of this system, even for long periods of time.

Figure 8

4. Discussion

The SVET analysis in the previous section was based on a semi-quantitative comparison of current density maps. It provided the spatial and time distribution of anodic and cathodic activities with the respective magnitudes. This is of invaluable importance for the description of the corrosion process and usually suffices when studying or ranking new systems.

It is possible to go further and attempt to extract more information from the SVET results. In this section we analyse the SVET data with simple statistical parameters and try to obtain information regarding the corrosion performance of the system under study. While doing so, the main sources of uncertainties and errors are identified and discussed. The criteria to compare the localised character of corrosion attack are also discussed in the second part.

4.1. Statistical analysis

Here an approach already experimented before is followed [20, 21]. The performance of different treatments can be compared by plotting together the values of the highest anodic and cathodic peak values, respectively, $j_{max\ peak,a}$ and $j_{max\ peak,c}$. When, as usual, there are several peaks or regions it may be better to use the average anodic or cathodic

current densities of each map. These average current densities can be calculated by the following equation,

$$j_{an/cat}^{map\ average} = \frac{\sum_{n=1}^{N} j_{n(an/cat)}}{N} \quad (1)$$

where $j_{an/cat}^{map\ average}$ stands for average anodic (or cathodic) current density of the analysed area, $j_{n(an/cat)}$ is the current density measured in each point of the map (considering only the positive ones, $j_{n(an)}$, for $j_{an}^{map\ average}$ and the negative ones, $j_{n(cat)}$, for $j_{cat}^{map\ average}$), and N is the number of points in the map.

Equation (1) should include only the significant points, i.e., those above the noise level to avoid current overestimation, especially in maps containing many points. The noise level can be determined from maps obtained in the same experimental conditions but without currents flowing in solution (no corroding sample). In such conditions the map should be a random collection of very small negative and positive currents scattered around zero. Figure 9 shows the point values of a map acquired in a Petri dish containing 0.05M NaCl using the same experimental parameters of the maps as in this work. The mean current was $\bar{x}$ = 0.082 μA cm^{-2} and the standard deviation was σ = 0.49 μA cm^{-2}. Figure 9 also shows $\bar{x}$±3σ, which is the recommended value in analytical chemistry for the limit of detection [22, 23]. The lines in Figure 9 show that using $\bar{x}$±σ renders significant too many noise points and with $\bar{x}$±3σ there is the risk of discarding many valid points. For this reason, we opted for a compromise and used a value of $\bar{x}$±2σ. As a consequence, only points with $|j|$ > 1 μA cm^{-2} were considered in equation (1).

Figure 9

Figure 10 plots the evolution of $j_{max\ peak,a}$, $j_{max\ peak,c}$, $j_{an}^{map\ average}$ and $j_{cat}^{map\ average}$ of the SVET maps for the three systems during the first month of immersion. It leads to the same trends concerning the corrosion results obtained from SVET maps in the previous section: the highest values belong to AA2024-T3, followed by **LDH-NO_3**, whereas **LDH-VO_x** presented very small values, near or within the noise level. One important aspect must be mentioned: the discrepancy between anodic and cathodic currents. Both currents should cancel out. This, however, only rarely occurs. There are several reasons that can explain this observation: i) the maps were obtained at 200 μm above the surface, not detecting the currents that flow below this level; ii) the maps only show the *z* component of the current (normal to the surface), missing the *x* and *y* components that may be significant and variable in different points of the sample; iii) the current that crosses the plane of measurement will surely cross it back in the opposite direction but everything outside the mapped area will be neglected; iv) current densities smaller than the noise level (around ±1 μA cm^{-2} for the conductivity of 0.05M NaCl) are not accounted for, in spite of their existence. Only in some favorable conditions SVET maps show even positive and negative values. Many times anodic currents are easier to be detected owing to their stronger localisation and consequent higher current density. Conversely, the movement of the SVET probe, and sometimes the vibration itself, may enhance the convective transport of O_2 to the surface and increase locally and momentarily the cathodic activity, precisely when the probe is measuring it, leading to an overestimation of the cathodic activities [24, 25].

Figure 10

4.2. Assessment of the degree of localised corrosion from SVET data

Corrosion rates are difficult to determine for localised corrosion, as in the present case. However, SVET can be very important to analyse the local intensity of corrosion currents and degree of localisation of attack.

There are two main ways of obtaining the total current of a sample, depending on the distribution depicted in the maps: discrete, well defined and well separated anodic peaks, or anodic and cathodic regions of irregular shape and size. In the first case, if the discrete anodic spots can be treated as point current sources, the current that gives origin to each one is given by:

$$I_{point\ source} = 2\,\pi\,r^2\,j_{SVET} \qquad (2)$$

where $I_{point\ source}$ is the current flowing from the point source in the metal surface, j_{SVET} is the current measured by SVET at a height r exactly above the point source and $2\,\pi\,r^2$ is the area of the hemisphere with radius r. The current density is a 3D vector. Exactly above the point source it coincides totally with the z component (x and y components are null at this exact position) and SVET can measure the total current density. In all other positions the z component gives just part of the current density. If the SVET maps have well defined and well separated anodic peaks and if their sources can be regarded as points, then the sum of all individual anodic currents $I_{point\ source}$ gives the total current (corrosion current) of the sample. The result of this approach is plotted in Fig. 11, for AA2024-T3 and **LDH-NO_3** specimens.

The existence of well-defined and well separated peaks is close to an ideal case. Often, SVET maps depict wide anodic and cathodic regions of irregular shape. The approach to determine the total current in these circumstances requires maps acquired close enough to the surface so that the current comes from the surface in a planar fashion. If this condition is met, the mapped currents in solution will be similar to the currents at

the metal surface and the total anodic current will be given by equation (1). This is also shown in Figure 11. In the present study the results from the two approaches are not so different. The values are between 0.3 and 0.8 μA for AA2024-T3 (area = 0.28 cm^2) and around 0.1 μA for **LDH-NO_3** (area = 0.20 cm^2), while for **LDH-VO_x** they were below the detection limit.

In general, the values given by SVET will be an underestimation. Besides, the currents flowing very close to the surface, between very small anodes and cathodes (uniform corrosion), will not be detected. The corrosion currents show a four- to ten-fold decrease for AA2024-T3 when coated by **LDH-NO_3** and an even higher decrease, but not quantified, by the **LDH-VO_x** layer.

Nevertheless the above said, we tried to compare the values of corrosion currents thus obtained with the values determined for systems involving the same aluminium alloy obtained by more traditional techniques as polarization techniques [13, 26, 27] and current converted weight loss [28] and the values are in close agreement, which validates the SVET results.

Figure 11

SVET measurements allow also to analyse the level of localised attack of a certain sample, since it becomes very clear where the anodic currents come from, i.e., the surface areas which have been attacked and the intensity of this local attack. However, the definition of a parameter that can evaluate the degree of localisation in different samples is very difficult. One of the reasons is the change in ‘active’ surface area of the exposed metal substrate as a function of time, an intrinsic challenge for the determination of corrosion rates when corrosion is not uniform. In this section we try to take this discussion forward, using the SVET data obtained for LDH films.

Let's consider the maps presented in Fig. 7, with a sample showing several active pits (bare AA2024-T3), a sample with just one single pit (**LDH-NO_3**) and another sample showing no corrosion (**LDH-VO_x**). Three different approaches were considered (Table 1). The first was simply the ratio of the highest to the average anodic current densities in the same map. A variant used was the mean value of all pits instead of the highest anodic current. The units are nondimensional and higher values indicate higher degree of corrosion localisation. A third and probably better parameter was based on the comparison of the current from localised sources (pits), $I_{local,a}$, with the total anodic current of the sample, $I_{map,a}$. These currents were calculated by summing the individual current densities of the points of interest (pits or total sample) and multiplying by the area corresponding to a single point [20, 21], as shown in the following equation, where *npi* corresponds to the number of points of interest,

$$I_{(local,a \text{ or } map,a)} = A_{point} \sum_{n=1}^{npi} j_n \quad (3)$$

The ratio $I_{local,a}$ / $I_{map,a}$ is the fraction of anodic current that comes from localised activity. The results of the analysis are presented in Table 1. The analysis based on the maximum peak currents indicates **LDH-NO_3** as the sample with higher level of localised corrosion. However, when comparing the anodic current coming from localised sources with the total anodic current in the map, it is found that the current from the pit in **LDH-NO_3** is only 51% of the total anodic current of this sample while in AA2024-T3 90% of the anodic current comes from the pits. The absence of currents in **LDH-VO_x** shows that there is no corrosion or it is small and uniform (not localised at the scale of measurement).

A parameter such as the degree of localised corrosion, combined with others that give a measure of corrosion extent, would be of valuable importance for definition of a more general factor of performance for alloys where localised corrosion is an issue. This is a

topic worth of attention in future works. SVET method is one of the most promising methods which can provide the important information on the localised corrosion currents.

5. Conclusions

Layered double hydroxide conversion films were grown on AA2024-T3 and characterized by different electrochemical techniques. Localised studies by SVET are in agreement with EIS results. The results show that thin LDH films work as effective protective layers for AA2024-T3 for long immersion times in NaCl solution, particularly when vanadates are intercalated. The level of protection achieved is even more remarkable considering that very low current densities were measured in artificial defects after one month of immersion.

In addition, the analysis of SVET current density maps allowed obtaining several quantitative factors. Furthermore, a parameter for the degree of corrosion localisation based on these factors was introduced and discussed. This parameter could be also used for other similar systems where the localised corrosion processes play a key role.

Acknowledgments:

This work was developed in the scope of the project CICECO-Aveiro Institute of Materials (Ref. FCT UID /CTM /50011/2013), financed by national funds through the FCT/MEC and when applicable co-financed by FEDER under the PT2020 Partnership Agreement. JT and SK thank FCT for researcher grants IF/00347/2013 and IF/00856/2013, respectively. Authors also thank FCT (Portugal) for project CONVPROTECT - PTDC/CTM-MAT/1515/2012 and the European Commission for

project H2020-MSCA-RISE-2014-645676-MULTISURF. Authors thank Dr. Eddy Domingues for the acquisition of SEM/EDS images.

References:

[1] M. Bethencourt, F.J. Botana, J.J. Calvino, M. Marcos, M.A. Rodriguez-Chacon, Corros. Sci. 40 (1998) 1803.

[2] P. Campestrini, H. Terryn, A. Hovestad, J.H.W. de Wit, Surf. Coat. Technol. 176, (2004) 365.

[3] R.L. Twite, G.P. Bierwagen, Prog. Org. Coat 33 (1998) 91.

[4] D. Wang, G.P. Bierwagen, Prog. Org. Coat. 64 (2009) 327.

[5] A.M. Cabral, W. Trabelsi, R. Serra, M.F. Montemor, M.L. Zheludkevich, M.G.S. Ferreira, Corros. Sci. 48 (2006) 3740.

[6] D.E. Tallman, G. Spinks, A. Dominis, G.G. Wallace, J. Solid State Electrochem. 6 (2002) 73.

[7] M. Rohwerder, S. Isik-Uppenkamp, C.A. Amarnath, Electrochim. Acta 56 (2011) 1889.

[8] W. Zhang, R.G. Buchheit Corrosion 58 (2002) 591.

[9] J. Tedim, M.L. Zheludkevich, A.N. Salak, A. Lisenkov, M.G.S. Ferreira, J. Mater. Chem. 21 (2011) 15464.

[10] J. Chen, Y. Song, D. Shan, E. Han, Corros. Sci. 53 (2011) 3281.

[11] J. Tedim, M.L. Zheludkevich, A.C. Bastos, A.N. Salak, A. Lisenkov, A.B. Oliveira, M.G.S. Ferreira, Electrochim. Acta 117 (2014) 164.

[12] J. Tedim, M.L. Zheludkevich, A.C. Bastos, A.N. Salak, A. Lisenkov, A.B. Oliveira, M.G.S. Ferreira, ECS Electrochem. Lett. 3 (2014) C4.

[13] K.D. Ralston, S. Chrisanti, T. L. Young, R. G. Buchheit, J. Electrochem. Soc. 155 (2008) C350.

[14] Q. Meng, T. Rampogal, G. S. Frankel, Electrochem. Solid-State Lett. 5 (2002) B1.

[15] G. Williams, H.N. McMurray, Electrochem. Solid-State Lett. 6 (2003) B9.

[16] R.G. Buchheit, H. Guan, S. Mahajanam, F. Wong, Prog. Org. Coat. 47 (2003) 174.

[17] R.L. Cook Jr, S.R. Taylor, Corrosion 56 (2000) 321.

[18] M. Iannuzzi, G.S. Frankel, Corros. Sci. 49 (2007) 2371.

[19] M.L. Zheludkevich, S.K. Poznyak, L.M. Rodrigues, D. Raps, T. Hack, L.F. Dick, T. Nunes, M.G.S. Ferreira, Corros. Sci. 52 (2010) 602.

[20] A.C. Bastos, M.L. Zheludkevich, M.G.S. Ferreira, Port. Eletrochim. Acta 26 (2008) 47.

[21] S. Kallip, A.C. Bastos, M.L. Zheludkevich, M.G.S. Ferreira, Corros. Sci. 52 (2010) 3146.

[22] D.A. Skoog, F.J. Holler, T.M. Nieman, Principles of Instrumental Analysis, 5th Ed, Saunders College Publishing, 1998, p.13.

[23] G.L. Long, J.D. Winefordner, Anal. Chem. 55 (1983) 712A.

[24] H.N. McMurray, D. Williams, D.A. Worsley, J. Electrochem. Soc. 150 (2003) B567.

[25] A.C. Bastos, M.C. Quevedo, M.G.S. Ferreira, Corros. Sci. 92 (2015) 309.

[26] H. Wang, R. Akid, Corros. Sci. 49 (2007) 4491.

[27] O. L.-Garrity, G.S. Frankel, Electrochim. Acta 130 (2014) 9.

[28] G. Williams, A.J. Coleman, H.N. McMurray, Electrochim. Acta 55 (2010) 5947.

CAPTIONS

Figure 1 - Scheme of the process for growth of LDH conversion films on AA2024-T3 (according to [9, 11]).

Figure 2 - SEM image of LDH deposited on AA2024-T3 and EDS maps for Al, Zn and N elements.

Figure 3 - Bode and Nyquist representations of EIS spectra of AA2024-T3 (a), AA2024-T3 coated with **LDH-NO_3** (b) and AA2024-T3 coated with **LDH-VO_x** (c) during immersion in 0.05 M NaCl.

Figure 4 - Equivalent electric circuits used to fit the EIS spectra.

Figure 5 – Evolution of the resistive parameters of the three systems obtained by numerical fitting of the impedance spectra.

Figure 6 - SVET maps of the AA2024-T3 bare substrate (a), AA2024-T3 coated with **LDH-NO_3** and AA2024-T3 coated with **LDH-VO_x** immersed in 0.05 M NaCl.

Figure 7 - (A) 3D SVET maps of the different systems after 1 month of immersion in 0.05 M NaCl.

Figure 8 - SVET maps and optical photographs of a sample of AA2024-T3 coated with **LDH-VO_x**, with two pin-hole defects.

Figure 9 - Noise level of measurements in 0.05M NaCl performed in a Petri dish with no sources of current present. Shown are the mean current ($\overline{x}$), the standard deviation (σ), 2σ and 3σ.

Figure 10 - Plots of highest anodic current density in the SVET maps (maximum peak height) (a) and the average current density in the map (b) for AA2024-T3, **LDH-NO_3** and **LDH-VO_x**.

Figure 11 - Total current in sample estimated by SVET.

Table 1 – Degree of corrosion localisation of samples AA2024-T3, **LDH-NO_3** and **LDH-VO_x**, shown in Figure 7, determined by three different criteria: ratio of the maximum peak current density in map and the average anodic current density, ratio of average of all peaks and average anodic current in map, ratio of the total anodic current from localised sources and the total anodic current density in the sample.

FIGURE 1

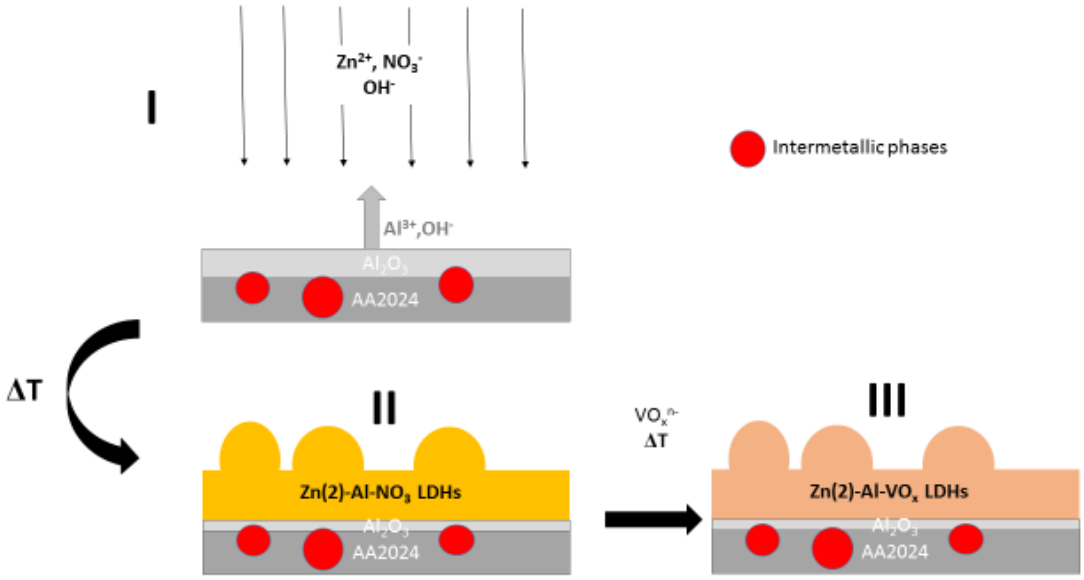
I
Zn^{2+}, NO_3^-
OH^-
Intermetallic phases
Al^{3+},OH^-
Al_2O_3
AA2024
ΔT
II
Zn(2)-Al-NO_3 LDHs
Al_2O_3
AA2024
VO_x^{n-}
ΔT
III
Zn(2)-Al-VO_x LDHs
Al_2O_3
AA2024

FIGURE 2

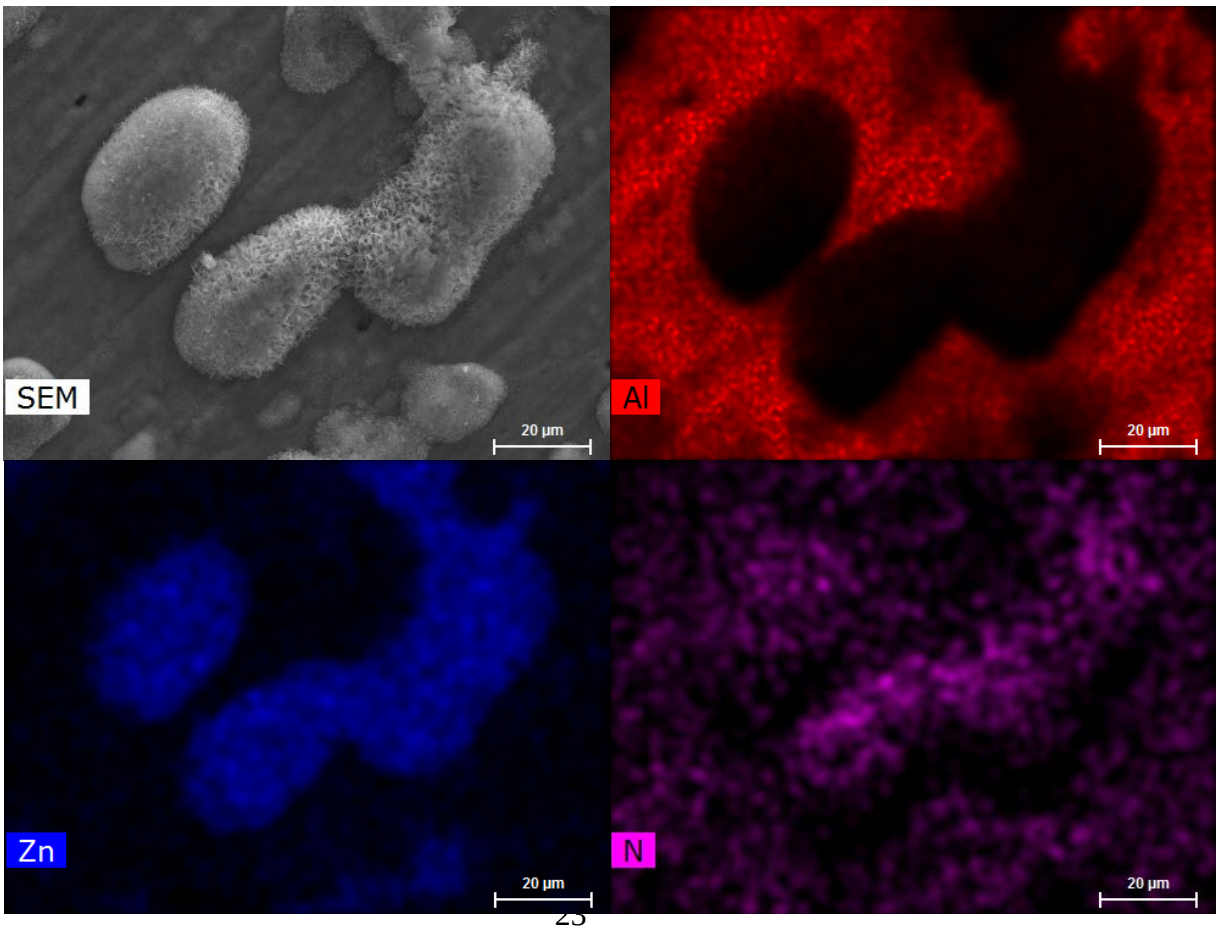

FIGURE 3

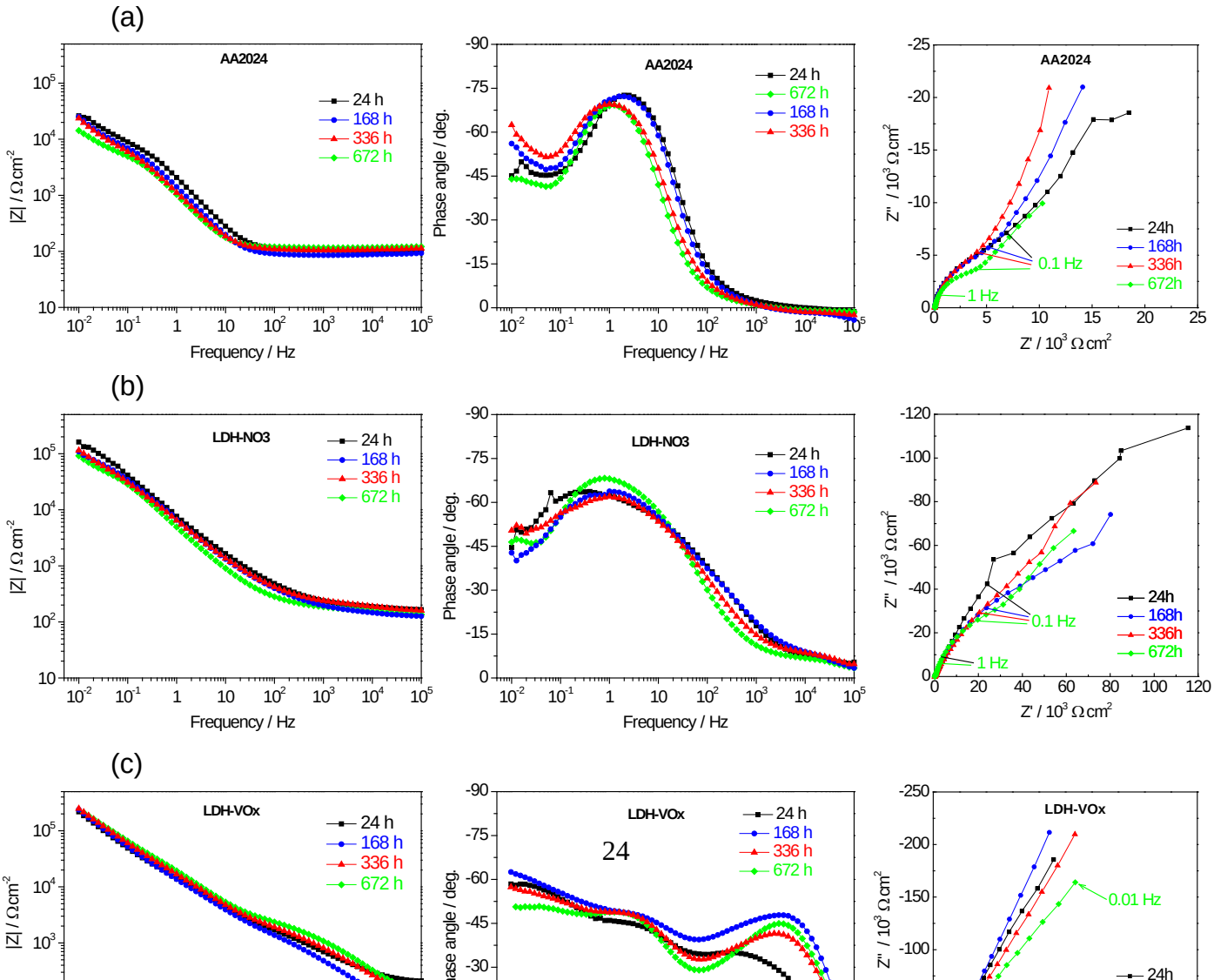
(a)
AA2024
24 h
168 h
336 h
672 h
|Z| / Ω cm²
Frequency / Hz
Phase angle / deg.
Z'' / 10³ Ω cm²
Z' / 10³ Ω cm²
0.1 Hz
1 Hz
(b)
LDH-NO3
(c)
LDH-VOx
24
0.01 Hz

FIGURE 4

(a)

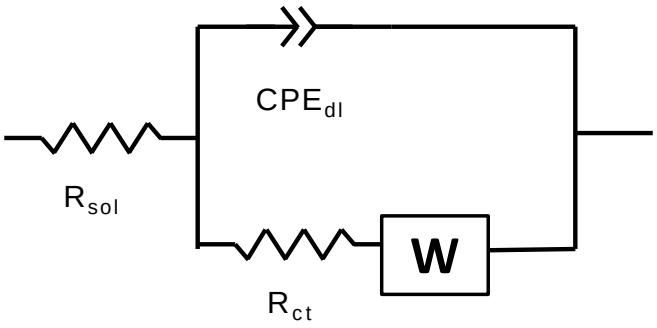

(b)

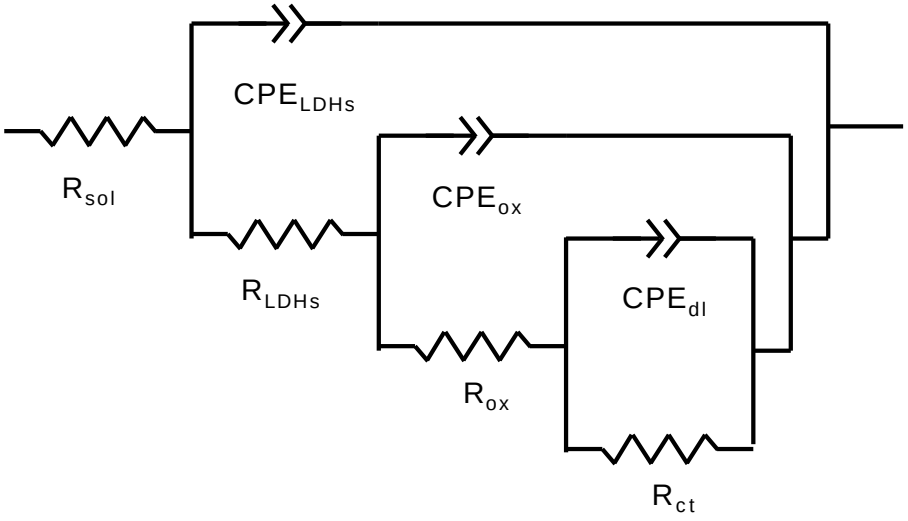

FIGURE 5

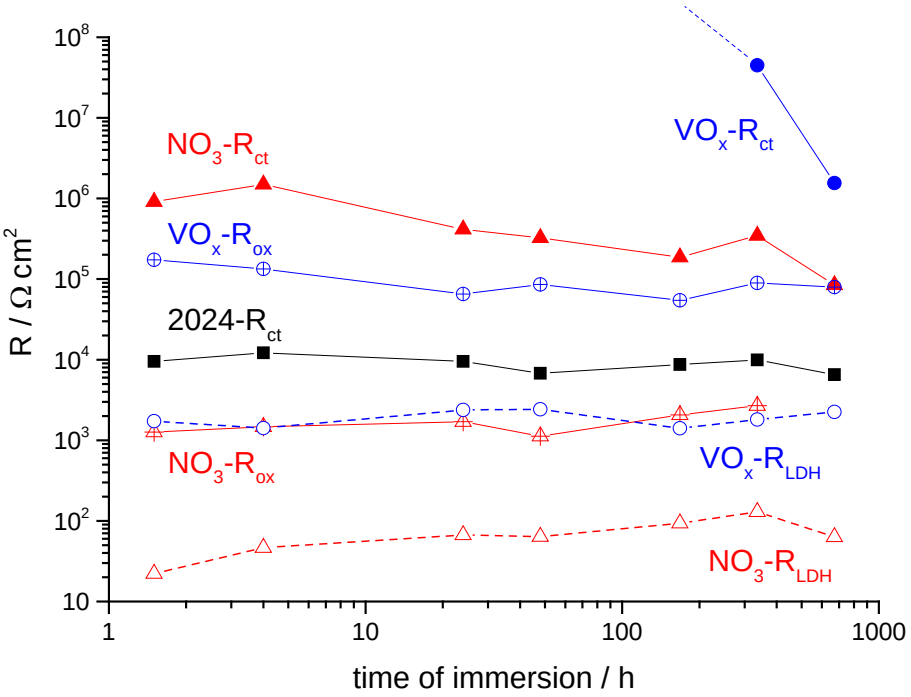
R / Ω cm2
time of immersion / h
NO3-Rct
VOx-Rct
VOx-Rox
2024-Rct
NO3-Rox
VOx-RLDH
NO3-RLDH
10
1
10
100
1000

FIGURE 6

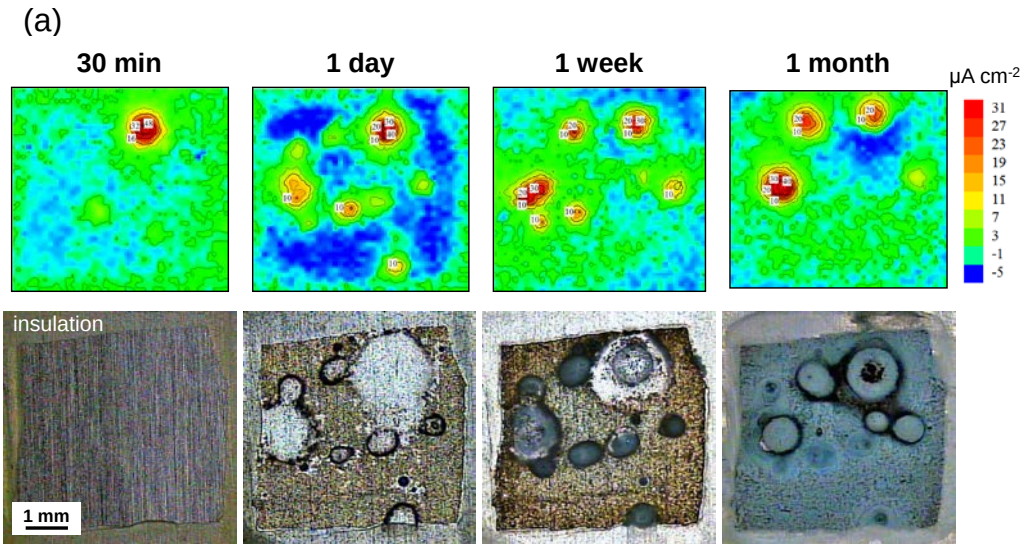
(a)
30 min
1 day
1 week
1 month
μA cm-2
31
27
23
19
15
11
7
3
-1
-5
insulation
1 mm

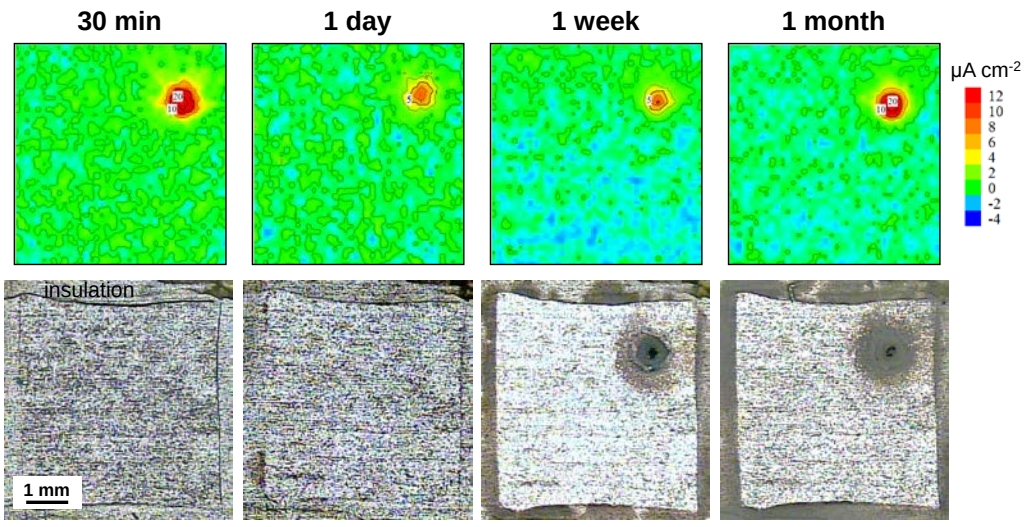
(b)
30 min
1 day
1 week
1 month
μA cm-2
12
10
8
6
4
2
0
-2
-4
insulation
1 mm

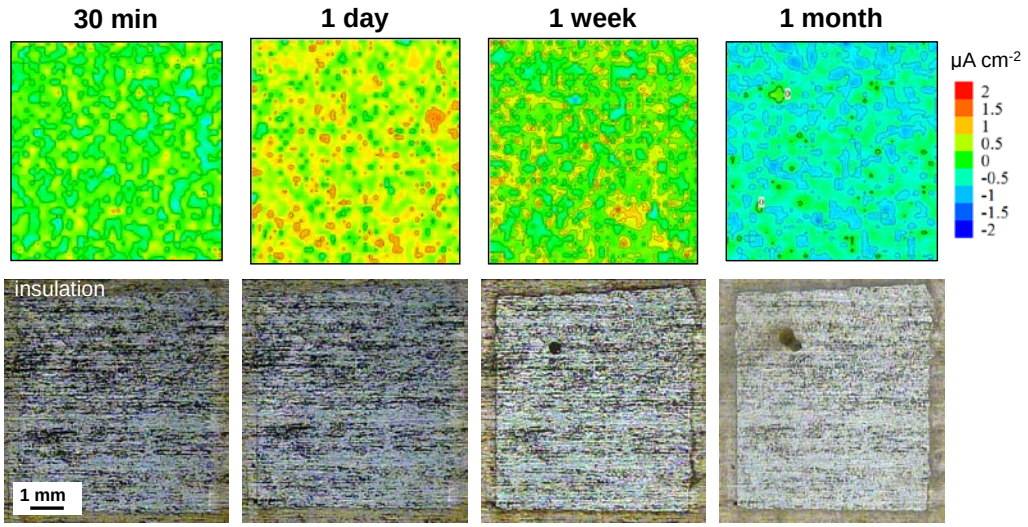
(c)
30 min
1 day
1 week
1 month
μA cm-2
2
1.5
1
0.5
0
-0.5
-1
-1.5
-2
insulation
1 mm

FIGURE 7

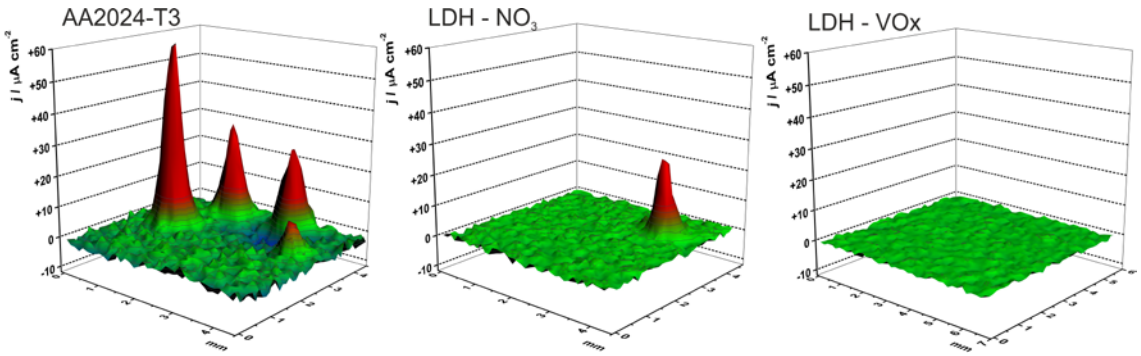

FIGURE 8

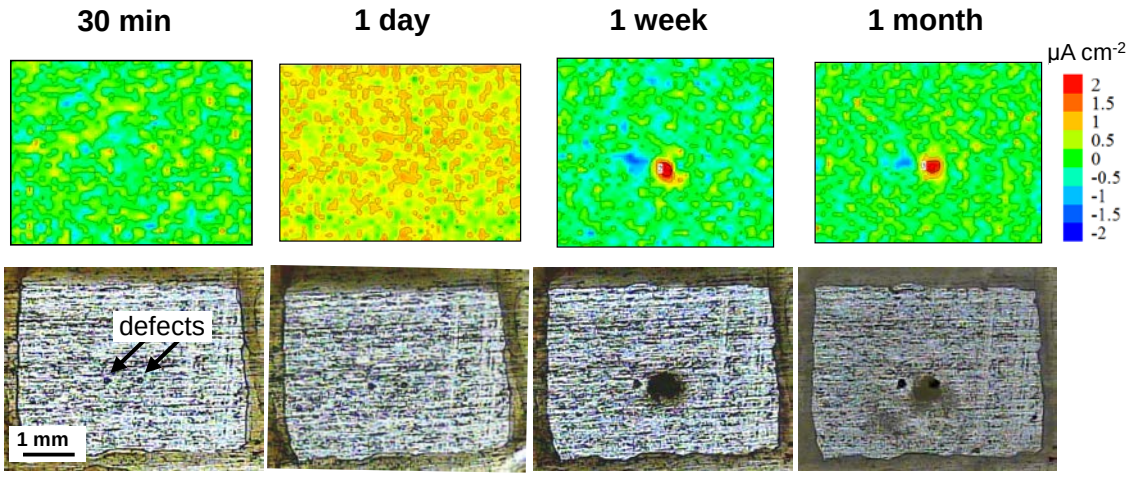

FIGURE 9

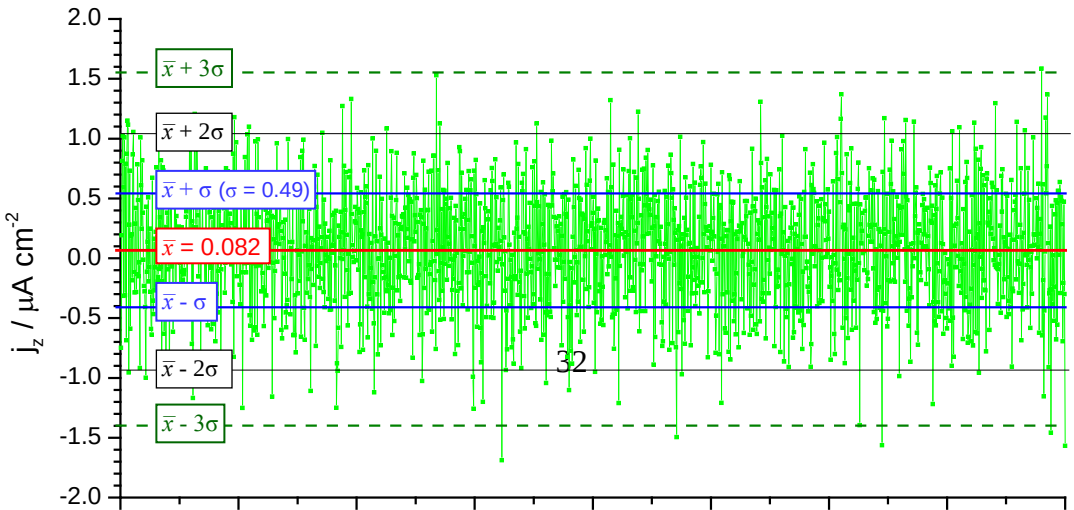
2.0
1.5
1.0
0.5
0.0
-0.5
-1.0
-1.5
-2.0
$\bar{x}$ + 3σ
$\bar{x}$ + 2σ
$\bar{x}$ + σ (σ = 0.49)
$\bar{x}$ = 0.082
$\bar{x}$ - σ
$\bar{x}$ - 2σ
$\bar{x}$ - 3σ
j_z / μA cm^{-2}

FIGURE 10

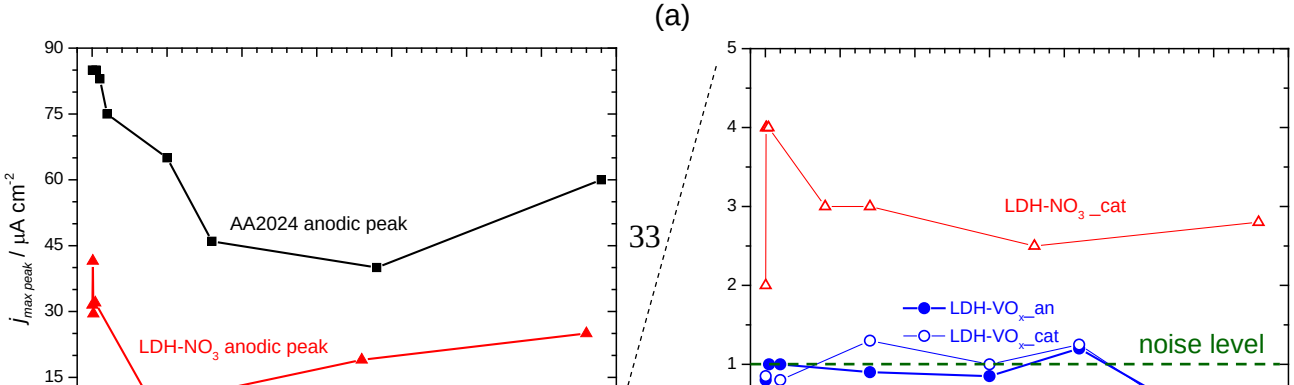
(a)
90
75
60
45
30
15
$j_{max\ peak}$ / µA cm^{-2}
AA2024 anodic peak
LDH-NO$_3$ anodic peak
33
5
4
3
2
1
LDH-NO$_3$_cat
LDH-VO$_x$_an
LDH-VO$_x$_cat
noise level

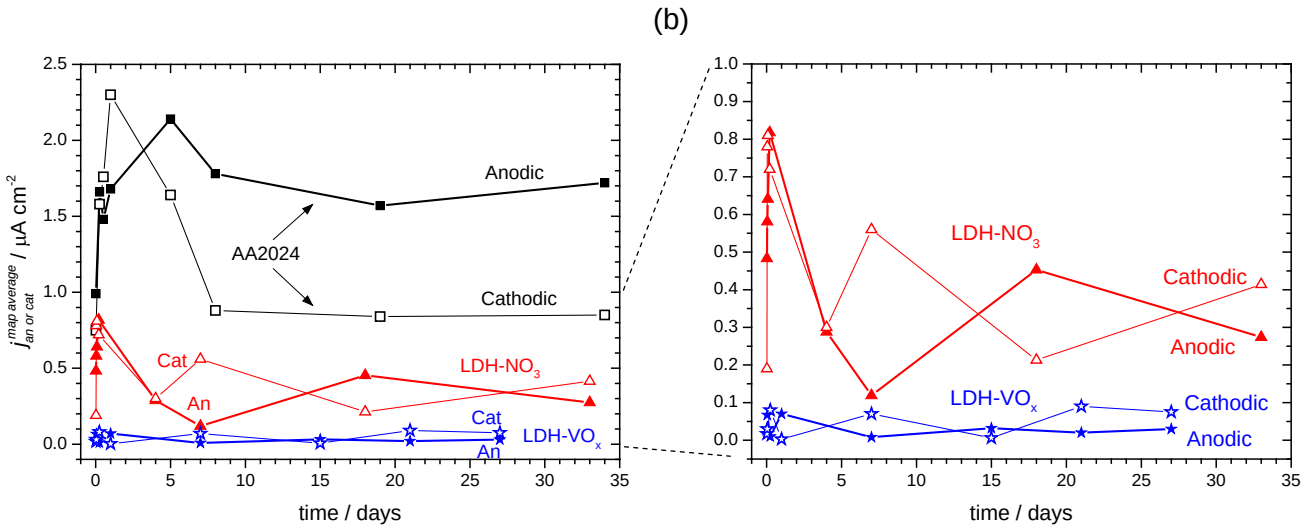
(b)
Anodic
AA2024
Cathodic
Cat
An
LDH-NO3
Cat
An
LDH-VOx
time / days
LDH-NO3
Cathodic
Anodic
LDH-VOx
Cathodic
Anodic
time / days

FIGURE 11

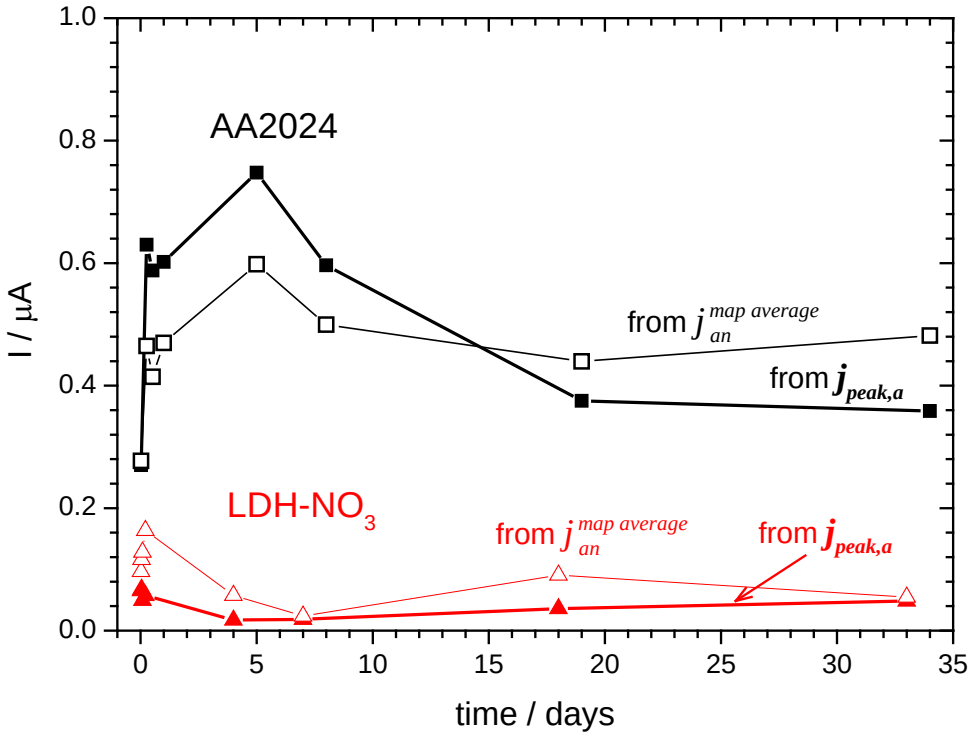
1.0
0.8
0.6
0.4
0.2
0.0
I / µA
AA2024
from $j_{an}^{map\ average}$
from $j_{peak,a}$
LDH-NO$_3$
from $j_{an}^{map\ average}$
from $j_{peak,a}$
0
5
10
15
20
25
30
35
time / days